Influence of Control Strategy on Measured Actuator Power Consumption in an Energy Storage Flywheel with Magnetic Bearings

Lawrence A. Hawkins
CalNetix, Inc.
363 Van Ness Way #401
Torrance, CA 90501
larry@calnetix.com

Mark Flynn
Center for Electromechanics - University of Texas
Mail Code R7000
Austin, TX 78712

Abstract

Minimizing power consumption is a key requirement in the system design of an energy storage flywheel. For magnetic bearing supported flywheels, synchronous power losses can be reduced by proper use of well established control approaches. Analysis and test results of amplifier and actuator power consumption are presented for several different control schemes: 1) a baseline gain scheduled compensator, 2) an improved compensator with reduced stiffness in the operating range, and 3) the baseline compensator with adaptive open loop control set up to minimize the synchronous currents. To compare the impact of the control changes, power usage and rotor displacement measurements were made on an operating 2.0 kWh flywheel in 2,000 rpm increments from rest to 40,000 rpm. Power consumption was derived from direct measurement of coil currents, coil voltages, and amplifier supply currents using a high-speed digitizer (2 MHz sample rate).

Introduction

A flywheel energy storage system (FESS) is under development as a possible replacement for the chemical battery storage system on the International Space Station (ISS). A flywheel system offers longer life, higher efficiency, and greater depth of discharge than batteries. Power for the ISS is generated by the station solar array system. The batteries supply station power during the 35 minute eclipse period of the 92 minute Earth orbit, and are recharged when power is available from the solar arrays (Kascak, et al, 2001). The flywheel under development is shown in Figure 1. The flywheel is designed to store 3.66 kWH at the 53,000 rpm maximum speed and deliver 1.35 kWh in a normal discharge cycle (one orbit).

Minimizing system power losses is an essential part of a successful flywheel energy storage system design, as losses reduce the net power that can be delivered. For this reason, all energy storage flywheels operate in a near vacuum to eliminate windage losses. Most designs also use magnetic bearings because of their low losses relative to other designs. For magnetic bearing systems operating in a vacuum, minimizing losses on the rotor is required, not only for good system efficiency, but also because the only heat transfer path off of the rotor is through radiation to the housing. Actuator (stator) losses, however, are responsible for a greater fraction of system losses, so reducing these losses can have a larger impact on overall system efficiency.
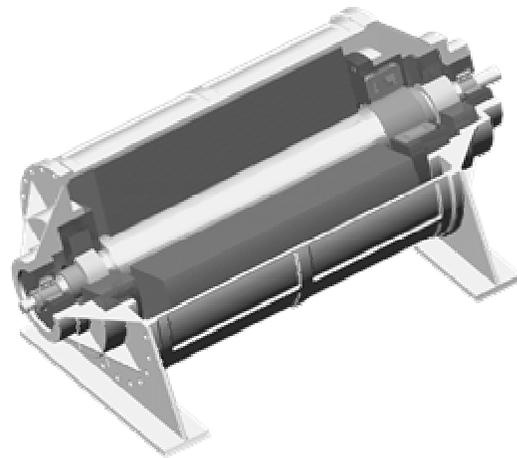
Figure 1. Cross-Section of the Flywheel Under Development.

The desire to improve system efficiency on the space station flywheel prompted this investigation. Since the space station flywheel is still under development, the experimental study reported here used an existing flywheel operated by the Center for Electromechanics (CEM) at the University of Texas (Hayes, et.al. 1998, Hawkins, et.al. 1999). The test flywheel, which is supported by permanent magnet bias magnetic bearings, can deliver 0.875 kWh during

a spin down from 40,000 rpm to 30,000 rpm. Power consumption measurements were made on this flywheel for three different control configurations: 1) baseline compensator, 2) modified baseline, compensator, having reduced stiffness between 32,000 rpm and 40,000 rpm, and 3) the baseline compensator, together with a current minimization adaptive open loop control (OLC) approach. The measurements are then compared to power consumption predictions.

Actuator Power Consumption Sources

A block diagram of the actuator coil and drive system used with the test flywheel is shown in Figure 2. Transconductance switching (PWM) power amplifiers are used to convert a command voltage signal from the DSP into a coil drive current. The DC overhead (bus) voltage that is supplied to the amplifier is switched using an H-bridge of power MOSFET devices. The required coil current is achieved by using a 3-state modulation scheme to control the duty cycle and state (on or off) of the MOSFETs in response to the command signal. Internal diodes across the MOSFETs provide a path for the coil current when the MOSFETs are switched off. The significant power losses generated in the amplifier are associated with: a) conduction losses in MOSFETs, b) switching losses in the MOSFETs, c) conduction losses in the diodes, d) diode recovery losses, and e) control devices on the amplifier. All but the amplifier control power requirements increase with coil current, and the switching losses also increase with bus voltage.
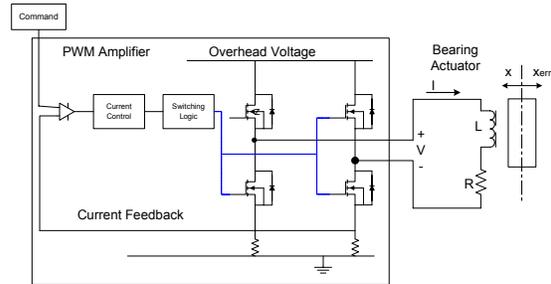

Figure 2. Actuator Coil and Amplifier Drive.

At low frequencies, the magnetic bearing can be represented by a coil with a series resistance. At higher frequencies the bearing model is improved by including a parallel resistance to model eddy currents. More sophisticated (and more accurate) models solve Maxwell's equations to more completely model eddy current effects (Meeker, et al, 1996).

Actuator stator losses are typically categorized as copper losses and core losses. The core losses are due to eddy currents and hysteresis effects generated in the bearing core. The dynamic flux field, due to dynamic current in the bearing coils, creates eddy currents in the conductive iron stator. Hysteresis, or the lag between the driving MMF and the magnetic flux, also causes power loss in the core when there is a dynamic coil current. Hysteresis losses were calculated from:

$$P_{hyst} = k_h f B_m^{1.8} V_{fe} \qquad (1)$$

where f is the excitation frequency, B_m is the flux density amplitude, V_{fe} is the volume of iron, and k_h is the hysteresis material constant. Eddy current losses were calculated from:

$$P_{eddy} = \frac{k_e e^2 f^2 B_m^2 V_{fe}}{\rho} \qquad (2)$$

where e is the lamination thickness, ρ is the resistivity of the lamination, and k_e is the eddy current constant. The values of k_h and k_e were calculated from 60 Hz and 400 Hz core loss data provided by the lamination manufacturer. One weakness of the predictions for this application is the lack of loss data above 400 Hz.

The copper losses are resistive losses in the bearing coil resistance. The voltage across the coil of a magnetic bearing actuator is:

$$V = L\frac{di}{dt} + Ri + K_b\frac{dx}{dt} \qquad (3)$$

where V is coil voltage, i is coil current, L is coil inductance, R is coil resistance, x is rotor displacement, and K_b is the voltage-velocity factor. Positive current, i, pulls the rotor away from equilibrium, and positive displacement, x, is displacement away from equilibrium (as in Vischer and Bleuler, 1990). The definitions of Equations 4 can be established from the angular relationships defined in Figure 3:

$$x(t) = X\cos(\omega t)$$
$$i(t) = I_{dc} + I\cos(\omega t + \varphi + 180°) \qquad (4)$$
$$v(t) = V_{dc} + V\cos(\omega t + \varphi + \theta + 180°)$$
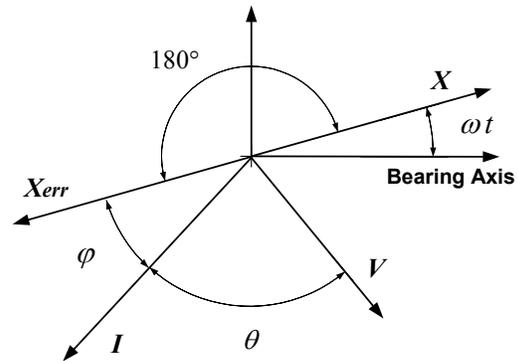

Figure 3. Phasor Relationship of Displacement, Error, Current and Voltage.

Substituting Equations 4 and the necessary time derivatives into Equation 3, the average power per cycle for frequency ω_k can be calculated by multiplying both sides by $i(t)$ and integrating over one cycle:

$$V_{dc}I_{dc} + \frac{1}{2}V_k I_k \cos(\theta) =$$

$$RI_{dc}^2 + \frac{1}{2}RI_k^2 + \frac{1}{2}K_b\omega_k X_k I_k \sin(\varphi_k + 180°) \quad (5)$$

The term on the left is the power into the coil from the amplifier. The first two terms on the right are the resistive copper losses. The last term is the power lost in the stator (+) or generated in the stator (-) by the rotor motion. The angle (φ+180°) is the angle between the actual coil current and the position of the rotor. If the current is driven mainly by a control signal to the amplifier, then at a frequency where the compensator phase lead, φ, is between 0° and 180°, (current leading the error), positive damping is being provided to the rotor. In these cases, sin(φ+180°) is negative, and Equation 5 says power is generated in the stator (removed from the rotor). This is consistent with conventional rotor/bearing systems (Thomson, 1981), where positive bearing damping removes power from the rotor, and negative damping delivers power to the rotor.

Control Approaches

Baseline Compensator. The baseline magnetic bearing control strategy used for the test flywheel is described in detail by Hawkins, et al, (1999). A gain-scheduled approach is used with four independent sets of control parameters (filter coefficients and gains). Each set of control parameters is applied in a different rotor spin speed range. The baseline magnetic bearing transfer function for the third speed range (32,000 rpm – 40,000 rpm) is shown in Figure 4. The magnetic bearing transfer function includes the dynamics of the position sensor, compensator (including a Pade approximation of the calculation phase delay), amplifier, and actuator.

Modified Baseline Compensator. The modified baseline compensator differs from the baseline compensator by some simple pole zero placement changes. These changes reduce the gain in the frequency range between 32,000 cpm and 40,000 cpm.

Open Loop Control with Baseline Compensator. Open loop cancellation (or adaptive vibration control) approaches have been widely described in the literature (Burrows, et al, 1988, Knospe, et al, 1994). There are numerous possible approaches, each with particular advantages. The choice depends on the system requirements and what is to be accomplished. The approach most often described adaptively minimizes synchronous displacement using a learned gain matrix that represents the force/displacement influence coefficients of the system. A second approach adaptively minimizes synchronous current, also using a learned gain matrix. A third approach adaptively minimizes the synchronous component of the error signal to the DSP, thereby reducing synchronous current (Larsonneur and Herzog, 1994).

The second and third approaches most directly minimize synchronous current, therefore reaction force and power consumption. The first approach can also reduce the net reaction force from the bearing, but at speeds well away from a critical speed can be expected to cause reaction force to increase.

The third approach was used to generate the test data reported here. This approach has much similarity to a tracking notch filter, and the similar limitation that it cannot be applied during the traverse of a mode This is because a synchronous force must be available from the bearings to counteract unbalance forces during the traverse of a mode. The adaptation can be frozen at a speed away from the mode, allowing a traverse without turning off the cancellation, but this is not as effective at a mode as the other approaches. The key reason for using this approach here is that it is the least computationally intensive, as it does not require a gain matrix. This is a distinct advantage at present for a space flywheel because of limitations on available processing power for space hardened DSPs.
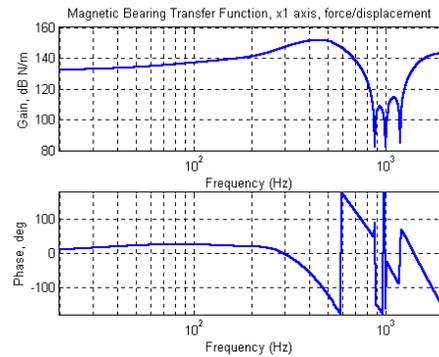
Figure 4. Baseline Magnetic Bearing (Force/Displacement) Transfer Function,

Measurement Approach

A high-speed Lecroy 6810 digitizer was used to record the coil voltages, coil currents, and rotor displacements. The digitizer can measure a differential signal of up to ±50 V. A sample rate of 2 Msamples/sec was used to capture the PWM voltage waveform (~22 kHz switching frequency) clearly. The coil voltage was measured using a differential voltage divider, with care taken to minimize capacitive loading on the voltage signal. The coil current was taken from the amplifier current monitor. The current monitor sensitivity and frequency response characteristics were calibrated against a LEM PR30 current probe, which was calibrated against a measurement resistor. The rotor displacements were sampled from the error signal to the DSP. The data was phase corrected for the low pass filtering in the sensor electronics. The total high voltage power was calculated from a measurement of voltage and current at the output of the high voltage power supply.

Data was taken in 2,000 rpm increments for the flywheel with the three different control situations

described above. The speeds used for each control setup are shown in Table 1.

Table 1. Control Cases

Case	Description	Speed Range (krpm)
1	Baseline Control	0 – 40
2	Baseline w/reduced gain	32 – 40
3	Baseline w/OLC	10 – 38

Test Results

Figure 5 is an example of the raw voltage and current data collected for each data set with the baseline compensator (Control Case 1). This data is a 2.5 ms time slice from the *X1* axis, 28,000 rpm data set. It is clear from both the voltage and current waveforms that the data is predominately synchronous. Also, several positive going cycles of the voltage waveform have a 100% duty cycle, indicating that the bearing *X1* axis is just at its slew rate limit.

A Fourier transform was performed for each data set to get amplitude and phase for voltage, current, and displacement components. The data sets each had 131,072 samples giving a time slice of 65.5 ms per data set. This limited the minimum frequency resolution to 15.25 Hz. In order to get synchronous amplitude information without leakage, each data set was truncated a small amount so that the synchronous frequency was an integer multiple of the Fourier transform frequency spacing. The phase between the voltage and current was obtained from a transfer function between the two signals.

Figure 6 shows the Fourier spectrums of the voltage and current for the data set of Figure 5. The voltage spectrum shows a synchronous amplitude of 160 V, the PWM switching frequency (22.75 kHz) and a small 3*synchronous component. The only significant signal in the current spectrum is the 3.7 A synchronous current.

Figure 7 shows a plot of the synchronous current versus speed for each of the radial axes. The data points were taken from the individual Fourier spectrums discussed above. The current has a peak on the *x1* and *y1* axes when traversing the conical rigid body mode at 20,000 rpm. There is a second peak at 32,000 rpm that occurs near the peak gain of the magnetic bearing transfer function (Figure 4).

Test results for Control Case 2 are similar, with synchronous currents and voltages that are 7% to 12% lower than for Control Case 1 in the tested speed range (from 32,000 rpm to 40,000 rpm).

Figure 8 shows Fourier spectrums of voltage and current for Control Case 3, OLC activated with the baseline compensator. The synchronous voltage is only about 8.5 volts, and the synchronous current is only 80 mA. The OLC algorithm has driven the synchronous amplifier command toward zero, which

also drives the synchronous current toward zero. The maximum synchronous current throughout the speed range was less than 150 mA. The synchronous coil voltage has a small *Ldi/dt* component, plus an EMF generated from the rotor motion in the bias flux field, $K_b \, dx/dt$ (Equation 3).
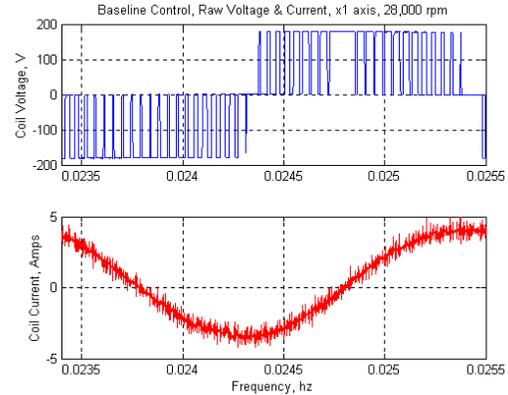
Figure 5. Raw Voltage and Current Time History, 28,000 rpm, *x1* axis, baseline control
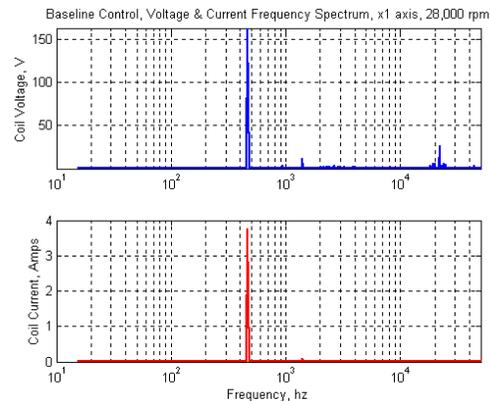
Figure 6. Voltage and Current FFT, 28,000 rpm, *x1* axis, baseline control
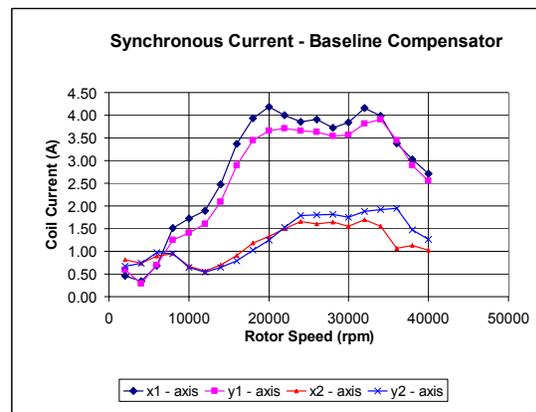
Figure 7. Synchronous Coil Currents, Baseline control.

The synchronous voltage measurements were somewhat inconsistent from speed to speed with the

OLC activated. This is because the coil voltage measurement sample rate, together with PWM switching frequency allows a resolution of only about 3 V on coil voltage, and the measured voltages were all below 11 volts. This was unfortunate, as the original plan was to determine K_b from the coil voltage and rotor displacement via Equation (3). As a substitute K_i, the roughly equivalent bearing force constant was used instead. Analog filtering before the digitizer will be used to refine the voltage measurement in future testing.
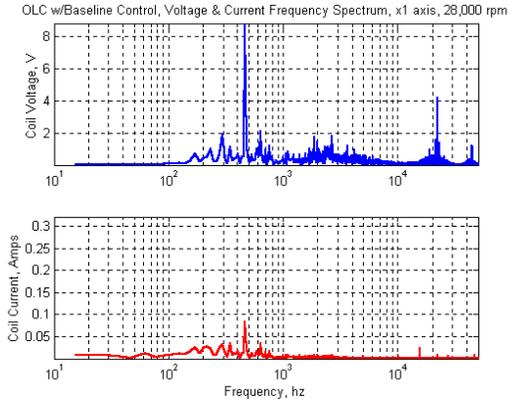

OLC w/Baseline Control, Voltage & Current Frequency Spectrum, x1 axis, 28,000 rpm

Figure 8. Voltage and Current FFT, 28,000 rpm, *x1* axis, OLC w/baseline control

Power Consumption Calculations from the Test Data

Power consumption was calculated from the voltage, current, and displacement data described above. Power into each bearing axis was calculated from:

$$P_{net} = V_{dc}I_{dc} + \frac{1}{2}\sum_{k=1}^{M}V_k I_k \cos(\theta_k) \qquad (6)$$

The sum was calculated for all harmonic frequencies up to 25 kHz (M~1650); however, in all cases, the only significant contribution was from the synchronous component. Power consumed (or generated) from rotor motion was calculated from:

$$P_{gen} = \frac{1}{2}\sum_{k=1}^{M}K_b \omega_k X_k I_k \sin(\varphi_k + 180°) \quad (7)$$

Power lost in the actuator from copper and core losses was calculated from:

$$P_{actuator} = P_{net} - P_{gen} \qquad (8)$$

Power lost in the amplifiers was calculated from:

$$P_{amplifier} = P_{supply} - P_{net} \qquad (9)$$

where the supply power, P_{supply}, was obtained by measuring DC voltage and current at the DC power supply to the amplifiers.

Figure 9 shows the power consumption data for Control Case 1 with the baseline compensator. Each curve is the sum of the four radial bearing axes (*x1,y1,x2,y2*). The peak supply power to the amplifiers is about 190 W at 32,000 rpm. The peak power delivered to the actuators through the amplifiers is about 95 W and the peak power consumed by copper and core losses is about 60 W, both at 32,000 rpm. Between 20,000 rpm and 38,000 rpm, power is delivered to the rotor via negative damping (the coil current lags the error signal), which is why the net power into the actuator is greater than the actuator losses. The amplifier power consumption rises with speed and current level also, but does not fall off much above 32,000 rpm when the current falls.
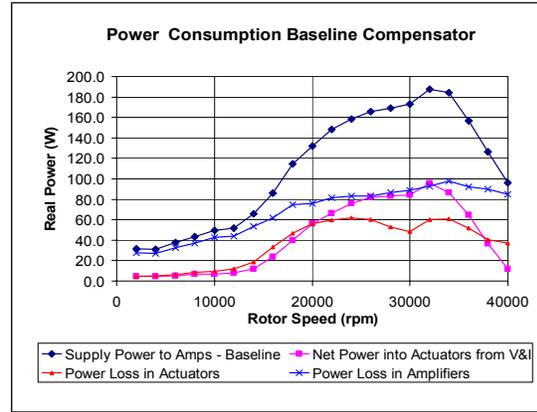

Figure 9. Actuator Power Consumption with Baseline Compensator.

Figure 10 shows a comparison of predicted and measured actuator power consumption. The predicted actuator power consumption was calculated by adding together the I^2R losses and the core losses from Equations 1 & 2. The current measurements described above and previously measured resistance and inductance values were used to get the results. Resistance and inductance were measured with a video bridge at several frequencies, using a 1 V signal. The correlation is quite good up to about 24,000 rpm, but between 30,000 and 40,000 rpm, the predicted results are about 30% higher than the measured values. Some possible contributors to the discrepancy are: 1) the k_h and k_e tend to be difficult to extrapolate above the highest tested frequency, 400 Hz in this case, and 2) K_i was used for K_b, but they are expected to deviate due to eddy current and hysteresis effects.

Power consumption data for the OLC case is shown in Figure 11. The net power into the actuator is only a few Watts. The supply power to the amplifiers is about 28 W at low speed, rising to 43 W at 40,000 rpm. Given that there is essentially no significant synchronous current (<150 mA max), an increase in amplifier power with speed was not expected. The 28 W in amplifier losses at low speed is mostly made up of hotel losses (for power conversion, control power, etc.), which were measured at about 4.5 W per axis, totaling 18 W for the four radial bearing axes.
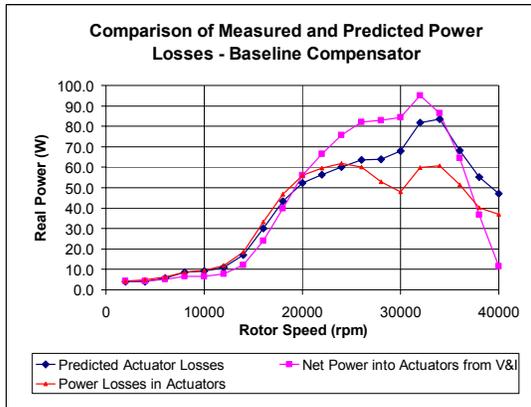
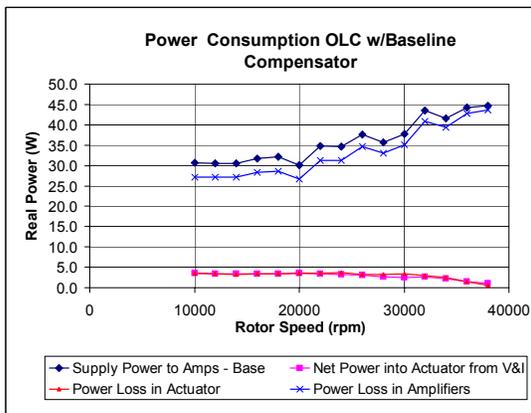**Figure 10. Comparison of Predicted and Extracted Actuator Power Consumption.**

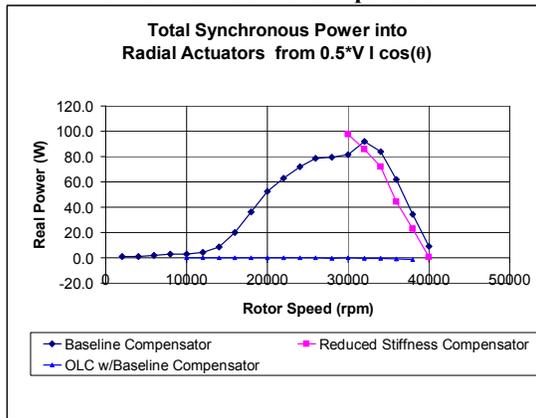**Figure 11. Actuator Power Consumption with OLC and Baseline Compensator.**

Figure 12. Comparison of Net Synchronous Power Into the Actuators.

Figure 12 is a comparison between the three control cases of synchronous power delivered to the radial actuators. Although reducing the gain of the transfer function at higher speeds did provide a marginal decrease in power consumption, using a current minimization OLC approach simply eliminated the synchronous power.

Conclusion

Actuator power consumption data was collected and analyzed for an energy storage flywheel, operating over a wide speed range. High frequency measurements were made of coil voltage, current and rotor displacement. Measurements were made for several control cases: two conventional compensators, and a conventional compensator together with an adaptive open loop cancellation (OLC) approach. The results show that a small decrease in power consumption was obtained by reducing control gain in a critical part of the operating range. However, the OLC approach essentially eliminated synchronous response to unbalance in the rotor, eliminating synchronous power consumption in the bearing throughout the applied speed range. Significant reductions in amplifier power consumption were also realized with the OLC. Future plans include expanding the testing to include two other variations of OLC. Improvements to the test technique will be made to improve the resolution of the coil voltage measurement.

Acknowledgement

References

Burrows, C.R., Sahinkaya, N., Traxler, A., Schweitzer, G., 1988, "Design and Application of a Magnetic Bearing for Vibration Control and Stabilization of a Flexible Rotor", 1st Intl. Symposium on Magnetic Bearings, ETH Zurich.

Hawkins, L.A., Murphy, B.T., Kajs, J.P., 1999, "Application of Permanent Magnet Bias Magnetic Bearings to an Energy Storage Flywheel", 5th Symp. on Magnetic Suspension Technology, Santa Barbara.

Hayes, R.J., Kajs, J.P., Thompson, R.C., Beno, J.H., 1998, "Design and Testing of a Flywheel Battery for a Transit Bus", SAE 1999-01-1159.

Kascak, P.E., Kenny, B.H., Dever, T.P., Santiago, W., Jansen, R.H., 2001, "International Space Station Bus Regulation with NASA Glenn Research Center Flywheel Energy Storage System Development Unit", 36th Intersociety Energy Conversion Engineering Conference, IECEC2001-AT-10, Savannah, GA, USA.

Larsonneur, R., Herzog, R.,1994, "Feedforward Compensation of Unbalance: New Results and Application Experiences", Proc. IUTAM Symposium. on the Active Control of Vibration, University of Bath, UK.

Meeker, D.C., Maslen, E.H., Noh, M.D., 1996, "An Augmented Circuit Model for Magnetic Bearings Including Eddy Currents, Fringing, and Leakage", IEEE Tran. Magnetics, Vol.32, No. 4.

Thomson, W.T., 1981, "Theory of Vibration with Applications", Prentice-Hall, Englewood Cliffs, New Jersey, USA, p. 68.

Vischer, D., Bleuler, H., 1990, "A New Approach to Sensorless and Voltage Controlled AMBs Based on Network Theory Concepts", 2nd International Symposium on. Magnetic Bearings, Tokyo.